ARL-TR-9193 ● MAY 2021

DEVCOM ARMY RESEARCH LABORATORY

Near-Field Target Scattering Characterization and Radar Modeling

by Traian Dogaru

Approved for public release; distribution is unlimited.

NOTICES

Disclaimers

The findings in this report are not to be construed as an official Department of the Army position unless so designated by other authorized documents.

Citation of manufacturer's or trade names does not constitute an official endorsement or approval of the use thereof.

Destroy this report when it is no longer needed. Do not return it to the originator.

ARL-TR-9193 ● MAY 2021



Near-Field Target Scattering Characterization and Radar Modeling

Traian Dogaru
Sensors and Electron Devices Directorate, DEVCOM Army Research Laboratory

Approved for public release; distribution is unlimited.

REPORT DOCUMENTATION PAGE

Form Approved
OMB No. 0704-0188

Public reporting burden for this collection of information is estimated to average 1 hour per response, including the time for reviewing instructions, searching existing data sources, gathering and maintaining the data needed, and completing and reviewing the collection information. Send comments regarding this burden estimate or any other aspect of this collection of information, including suggestions for reducing the burden, to Department of Defense, Washington Headquarters Services, Directorate for Information Operations and Reports (0704-0188), 1215 Jefferson Davis Highway, Suite 1204, Arlington, VA 22202-4302. Respondents should be aware that notwithstanding any other provision of law, no person shall be subject to any penalty for failing to comply with a collection of information if it does not display a currently valid OMB control number.
PLEASE DO NOT RETURN YOUR FORM TO THE ABOVE ADDRESS.

1. REPORT DATE *(DD-MM-YYYY)*	2. REPORT TYPE	3. DATES COVERED (From - To)
May 2021	Technical Report	March 2021–April 2021

4. TITLE AND SUBTITLE
Near-Field Target Scattering Characterization and Radar Modeling

5a. CONTRACT NUMBER

5b. GRANT NUMBER

5c. PROGRAM ELEMENT NUMBER

6. AUTHOR(S)
Traian Dogaru

5d. PROJECT NUMBER

5e. TASK NUMBER

5f. WORK UNIT NUMBER

7. PERFORMING ORGANIZATION NAME(S) AND ADDRESS(ES)
DEVCOM Army Research Laboratory
ATTN: FCDD-RLS-ES
2800 Power Mill Road
Adelphi, MD 20783-1138

8. PERFORMING ORGANIZATION REPORT NUMBER
ARL-TR-9193

9. SPONSORING/MONITORING AGENCY NAME(S) AND ADDRESS(ES)

10. SPONSOR/MONITOR'S ACRONYM(S)

11. SPONSOR/MONITOR'S REPORT NUMBER(S)

12. DISTRIBUTION/AVAILABILITY STATEMENT
Approved for public release; distribution is unlimited.

13. SUPPLEMENTARY NOTES
ORCID ID(s): Traian Dogaru, 0000-0002-1091-4928

14. ABSTRACT

This report develops near-field radar modeling techniques designed to produce the power-calibrated radar-received signal for arbitrary antennas and target configurations, based on computational electromagnetic simulations. The near-field radar cross-section concept is formulated together with its evaluation for simple-shape targets. Subsequently, we develop a general form of the radar equation that preserves the signal's phase, the impact of near-field geometry, and the polarimetric coupling effects between the antenna patterns and target scattering. These concepts are brought together in a practical method of simulating complex near-field radar sensing scenarios with the AFDTD modeling software. Numerical validation examples are presented, emphasizing the differences between the near- and far-field radar operational regimes.

15. SUBJECT TERMS
radar modeling, target scattering, radar cross section, near-field radar, radar equation

16. SECURITY CLASSIFICATION OF:			17. LIMITATION OF ABSTRACT	18. NUMBER OF PAGES	19a. NAME OF RESPONSIBLE PERSON
a. REPORT	b. ABSTRACT	c. THIS PAGE			Traian Dogaru
Unclassified	Unclassified	Unclassified	UU	30	19b. TELEPHONE NUMBER (Include area code) (301) 394-1482

Standard Form 298 (Rev. 8/98)
Prescribed by ANSI Std. Z39.18

Contents

List of Figures iv

1. Introduction 1

2. The Near-Field Radar Cross Section 2

3. A General Formulation of the Radar Equation 7

4. Near-Field Target Scattering Characterization Using the AFDTD Modeling Software 12

5. Numerical Examples 15

6. Conclusions 20

7. References 22

List of Symbols, Abbreviations, and Acronyms 23

Distribution List 24

List of Figures

Fig. 1 Comparison of the near-field and far-field RCS of circular plate of radius 0.5 m at a 5-m range, as a function of frequency 5

Fig. 2 Geometry of the near-field radar-sensing configuration used for validating the indirect near-field RCS calculation via the dipole method described in Section 4 16

Fig. 3 Comparison of electric field magnitudes at the receiver obtained by the direct and indirect methods: (a) E_x component; (b) E_y component; and (c) E_z component 18

Fig. 4 Comparison between the near-field and far-field RCS of a rectangular plate of dimensions 1 m × 0.6 m, computed by AFDTD simulations for (a) V-V (θ–θ) polarization; (b) H-H (ϕ–ϕ) polarization; (c) V-H (θ–ϕ) polarization; and (d) H-V (ϕ–θ) polarization 19

Fig. 5 Comparison between the near- and far-field RCS of a circular plate of radius 0.5 m at 5-m range, computed analytically and by AFDTD simulations 20

1. Introduction

The Electromagnetic (EM) Modeling Team at the US Army Combat Capabilities Development Command (DEVCOM) Army Research Laboratory (ARL) has a long track record of developing advanced simulations of radar scattering for a wide variety of complex sensing scenarios for the purposes of radar system analysis, performance prediction and optimization, and understanding the underlying EM phenomenology. Throughout this work, the team has been using several EM modeling software packages, such as AFDTD[1,2] (developed entirely at the DEVCOM Army Research Laboratory), Xpatch[3] (developed under Air Force funding), and Feko[4] (commercial software). All these codes can handle both far- and near-field radar-scattering scenarios, depending on the sensing configuration under investigation.

Traditionally, when analyzing a radar system, the designer assumes that the target and radar antenna are in the far-field region with respect to one another. This assumption simplifies many of the equations involved in analysis and allows one to precisely define quantities such as antenna directivity and radar cross section (RCS). As a result, most of the theory presented in radar textbooks relies on far-field configurations. Following this tradition, the majority of our team's simulation efforts in the past have used the EM software packages in the far-field mode, which is easier to handle and more computationally efficient than the near-field mode, since it does not have to explicitly include the radar antennas in the model.

However, many modern radar applications do not conform to the far-field model. The three major departures from this model consist of (1) spherical instead of planar radar wavefronts in the target area; (2) nonuniform antenna patterns in the target area; and (3) polarimetric coupling via target scattering for non-boresight antenna look angles. Typical examples of these applications are short-range radar configurations, such as sensing-through-the-wall (STTW) and ground-penetrating radar (GPR), which operate at low frequencies, with wide bandwidth waveforms and wide beam antennas. More generally, the analysis of any strip-map synthetic aperture radar[5] (SAR) system operating with wide-beam antennas must take into account all three near-field effects previously mentioned. Another application requiring the near-field treatment is imaging with millimeter-wave radar,[6] where the wavefront curvature has a major impact on the image formation procedure at any practical operational range.

To obtain realistic simulations of these radar scenarios, our team has created near-field models of the scenes under investigation, which include both the radar antennas and the target area. Although these models have generally provided

important phenomenological information to the radar designers, two shortcomings have limited their usefulness in the past. The first issue is the limited number of built-in antenna types that can be accommodated by some of the EM modeling software packages. For instance, AFDTD can only include dipole or rectangular aperture antennas in its near-field simulations. The integral equation solver in Feko can incorporate full-scale antenna models; however, combining those with arbitrary target models in one single radar scenario simulation is very difficult to achieve for any useful practical application.

Another problem is the lack of calibration of the radar-received signals in terms of power. This stems from the fact that the antenna excitation is not typically set to produce a radiated power of 1 W in the EM simulation software. One should note that calibrated power calculations represent a very important result of radar modeling from the system designer's point of view. In far-field modeling scenarios, this type of calculation is readily achievable in post-processing via the radar equation.[7] However, their near-field counterparts are more difficult to handle and require some modifications of the classic radar equation.

If one could create a complete calibrated model of the radar-sensing scenario including the actual transmitter (Tx) and receiver (Rx) antennas, as well as the target area, that model would provide all the relevant information about the scenario. However, as already discussed, such models are difficult to achieve with currently available EM solvers. Therefore, indirect methods based on existing solvers need to be developed to produce calibrated data in near-field radar scenarios involving arbitrary antenna types; this constitutes the main goal of the current investigation. The emphasis is on the AFDTD software, which is our team's most frequently used radar modeling tool.

This report is organized as follows. In Section 2, we discuss the concept of near-field RCS and derive expressions for some simple shape targets. Section 3 reformulates the traditional radar equation for general sensing scenarios. In Section 4, we develop methods for RCS and radar power calculations using AFDTD near-field models. These methods are illustrated with numerical examples in Section 5. We draw conclusions in Section 6.

2. The Near-Field Radar Cross Section

In this section, we discuss the near-field RCS definition and its analytic formulas for several simple target shapes. This material draws heavily from a paper by Pouliguen et al.,[8] which contains full derivations of the RCS analytic expressions (those derivations are not repeated in this report). However, the subsequent

interpretation of those results in the context of the radar equation is an original contribution of this study.

The far-field definition of RCS is[9]

$$\sigma_{FF} = \lim_{R\to\infty} 4\pi R^2 \frac{W_s}{W_i} = \lim_{R\to\infty} 4\pi R^2 \frac{|E_s|^2}{|E_i|^2} = \lim_{R\to\infty} 4\pi R^2 \frac{|H_s|^2}{|H_i|^2}. \quad (1)$$

In this equation, $W, |E|$ and $|H|$ are the power density, electric field magnitude, and magnetic field magnitude, respectively, with the subscript *i* standing for "incident on the target", and the subscript *s* for "scattered at the receiver". Note the $R \to \infty$ limit (*R* stands for range), which is characteristic to far-field scenarios. For near-field geometries, we remove this limit and write the general RCS equation as[8]

$$\sigma = 4\pi R^2 \frac{W_s}{W_i} = 4\pi R^2 \frac{|E_s|^2}{|E_i|^2} = 4\pi R^2 \frac{|H_s|^2}{|H_i|^2}. \quad (2)$$

One of the first issues with the general definition of the near-field RCS is how we define the incident field on the target. In the far-field case, where we work with plane waves, this quantity is well defined; however, in the near-field case, the incident electric field vector $\mathbf{E}_i$ can vary across the target extent in phase, magnitude, and direction. (These variations correspond roughly to the three departures from the far-field model mentioned in the Introduction, respectively.) Since only the magnitude matters in the RCS calculation, we can pick a reference point on the target (similar to the "phase center" of an antenna) and consider that the incident field has the same magnitude at any point on the target as at the reference point. In effect, we assume that the wave incident on the target is locally a uniform spherical wave emanating from the radar antenna. This situation amounts to neglecting the antenna pattern magnitude variations across the target and is typically a reasonable assumption for most radar scenarios, except for cases where we deal with very large targets or very short radar-target ranges.

In their paper, Poulinguen et al.[8] employ the physical optics (PO) method to perform analytic calculations of the near-field RCS of a circular and a rectangular plate at normal incidence. In the following paragraphs, we limit the discussion to monostatic radar. Additionally, all the targets considered in this section are made of perfect electric conductor (PEC). One should note that the PO method is approximate and typically accurate only in the high-frequency regime. Moreover, the near-field analytic calculations can only be performed for very particular shapes and incidence angles, and would be almost impossible to carry out for more

complex situations, such as oblique incidence. Therefore, these results have very limited practical applications. However, it is instructive to discuss these results, because they reveal some important aspects of the near-field RCS, which differ from the traditional far-field RCS concept.

The RCS formula obtained for the circular plate of radius a, which is the simplest case for near-field geometry, can be written as

$$\sigma = 4\pi R^2 \sin^2\left(\frac{ka^2}{2R}\right) = 2\pi R^2\left[1-\cos\left(\frac{ka^2}{R}\right)\right], \tag{3}$$

where $k = \frac{2\pi f}{c}$ is the wave number and f is the frequency. For reference, the far-field RCS formula for the same plate at normal incidence is

$$\sigma_{FF} = \frac{4\pi A^2}{\lambda^2} = \pi k^2 a^4 . \tag{4}$$

where A is the target area and $\lambda = \frac{2\pi}{k}$ is the wavelength. This result can be easily obtained from Eq. 3 in the limit $R \to \infty$.

There are two striking aspects where the near-field RCS differs from the far-field RCS: (1) the near-field RCS depends on the range R, whereas the far-field RCS depends only on target size and frequency; (2) the near-field RCS exhibits an oscillatory nature as a function of range (R), target size (a), and frequency (k), whereas the far-field RCS for the same target and incidence angle increases monotonically with size and frequency.

For a fixed size plate at a fixed range, we obtain the following maximum value of the near-field RCS as we vary the frequency: $\sigma_{\max} = 4\pi R^2$. The same limit applies if we keep the frequency and range fixed and vary the plate size. At first, the fact that the RCS should depend on range seems unusual and raises the question whether this increase with range is in some way unbounded. However, this should not be a reason for concern; in fact, one can look at the increase of RCS with range as an effect of the way the RCS is defined. To interpret this result, we notice the following:

1) One can show that as long as the near-field condition is satisfied ($R < \frac{8a^2}{\lambda}$), the near-field RCS is always smaller than the far-field RCS.

2) As the range keeps increasing, we transition into the far-field regime, and then the near-field and far-field RCS formulas converge to the same value.
3) The significance of the RCS can only be properly understood in the context of the radar equation, as explained in a subsequent paragraph.

Two simple numerical examples demonstrate these aspects. At Ka-band (35 GHz) and R = 1000 m, σ_{max} is 71 dBsm, whereas for R = 200 m, σ_{max} is 57 dBsm (remember that these quantities are independent of the plate size). We can compare these values with the far-field RCS of a 2.5-m-radius circular plate, which is 78 dBsm, or greater than both near-field σ_{max} values (and in turn does not depend on range).

The graph in Fig. 1 compares the near-field and far-field RCS of a circular plate of radius 0.5 m at a 5-m range (fixed) as a function of frequency. For this geometry, we are in the far field only at the lowest end of the frequency range, where the two RCS curves coincide. As the frequency increases, the two curves diverge, and the near-field RCS displays an oscillatory variation, with a maximum given by $4\pi R^2$, or approximately 25 dBsm.

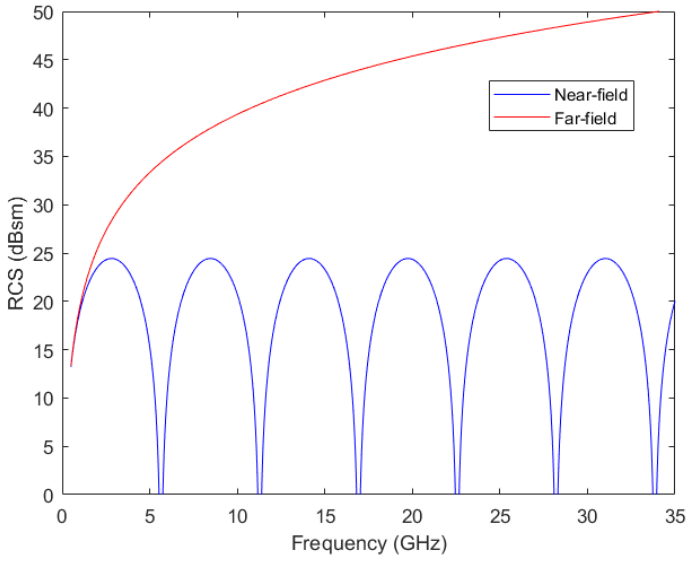

Fig. 1 Comparison of the near-field and far-field RCS of circular plate of radius 0.5 m at a 5-m range, as a function of frequency

The RCS evaluation is most relevant when used in conjunction with the radar equation. According to this equation, the radar-received power is proportional to $\frac{\sigma}{R^4}$.[7] When $\sigma \sim R^2$ (as for a plate in the near field), the range dependence in the radar-received power goes as $\frac{1}{R^2}$ instead of $\frac{1}{R^4}$; apparently, this says we are receiving larger power from the target in the near-field than in the far-field case.

However, that is not the case when all factors in the equation are taken into account—the received power in the near field is always smaller than that received in the far field, all other quantities being kept equal.

The next example considered by Pouliguen et al.[8] is a flat square plate with side *a* at normal incidence. The PO derivation for that case is much more complicated than for the circular plate and the resulting near-field RCS does not display the same well-defined oscillations. In fact, this RCS tends to a limit value as we increase the frequency, which is $\lim_{f\to\infty}\sigma = \pi R^2$. The complete RCS formula for the square plate at normal incidence is

$$\sigma = 4\pi R^2\left[\frac{1}{4}+2X+X^2-X\sin\left(\frac{1}{\pi X}\right)-\sqrt{2X}\left(1+2X\right)\sin\left(\frac{\pi}{4}-\frac{1}{2\pi X}\right)\right], \quad (5)$$

where $X=\frac{R\lambda}{\pi^2 a^2}$. A careful examination of this formula reveals that it contains terms in the following powers of *R*: $R^2, R^3, R^{3.5}$ and R^4. The key thing to understand when analyzing the formula is that as long as we are in the near-field regime, the *lowest-power* term in *R* (which in this case is R^2) is the *dominant* one. Consequently, upon inserting the RCS formula into the radar equation, the rectangular plate produces a radar-received power that displays the same-order variation with range as the circular plate, proportional to $\frac{1}{R^2}$.

In addition to the two targets considered so far, we also investigated the interesting case of a target with one large dimension, consistent with near-field geometry, and one small dimension, consistent with far-field geometry (note this type of target was not discussed by Pouliguen et al.). An example of such a target is a long straight wire. In this calculation, we assume a rectangular plate with the long side *a* and the short side *b*, at normal incidence. The PO method yields

$$\sigma = \frac{2b^2}{\lambda}\left(\pi R+\frac{4R^2}{ka^2}+\frac{2\sqrt{\lambda}R^{1.5}}{a}\left(\sin\left(\frac{ka^2}{4R}\right)+\cos\left(\frac{ka^2}{4R}\right)\right)\right). \quad (6)$$

Once again, as long as we are in the near field with respect to the long side, the lowest-power term in *R* is the dominant one. In this case, this term is simply proportional to *R*, not R^2 (as in the previous case of a plate of "balanced dimensions"). Consequently, when inserted into the radar equation, this RCS

produces a range dependence proportional to $\frac{1}{R^3}$. A high-frequency limit also applies to this near-field RCS, which is $\lim_{f\to\infty}\sigma = \frac{2\pi b^2 R}{\lambda}$.

The phenomenological explanation of the fact that the far-field RCS of a flat plate at normal incidence may exceed its near-field counterpart by a large margin has to do with the coherence of the scattered field across the target extent. Thus, a plane wave (characterizing the far-field case) at normal incidence to the plate has wave-fronts conforming perfectly to the scattering surface, which creates coherent returns from all points on the surface. On the other hand, a spherical wave (characterizing the near-field case) reaches different points on the flat surface with different phases, which reduces the coherence of returns from these points.

Nevertheless, one should not attempt to generalize these results to targets of arbitrary shapes or oblique incidence scenarios. Although differences between the far- and near-field RCS exist in most cases, there is no obvious reason to expect the far-field to exceed the near-field value, and certainly not by a large margin. This effect has to do with the loss of coherence in target scattering for those general scenarios, in both far- and near-field geometries. The simulations in Section 5 of this report support this statement.

The main usefulness of the results obtained in this section consists of establishing an upper bound for the target RCS in a near-field radar-sensing scenario, when the target dimensions are not precisely known. As already shown, this upper bound does not depend on the target dimensions, but only on range. This maximum RCS value is an important parameter in the front-end design of the radar receiver, which must avoid saturation of the amplifier for proper operation.[7]

3. A General Formulation of the Radar Equation

A major goal of radar system modeling is the evaluation of the radar transmitter power required to achieve a given signal-to-noise ratio. The traditional tool for this analysis is the radar equation. However, the classic radar equation (written in terms of transmitted and received powers) has some major shortcomings, the most obvious one being that it does not account for the radar signal's phase. Consequently, we cannot directly use the conventional form of the radar equation to analyze systems that perform coherent processing, such as SAR, range-Doppler, space-time adaptive processing, etc.[10] The typical way to account for coherent processing when evaluating the power is via certain factors representing the coherent processing gain. This very coarse procedure may work reasonably well for point–target-type analysis but is completely inadequate for more complex

modern radar-sensing scenarios, such as those involving ultra-wideband (UWB), wide-angle SAR imaging of complex-shaped targets. These are exactly the kind of scenarios we have been typically investigating in our advanced computer models at ARL; therefore, our processing tools must go beyond the radar equation to fully exploit the information contained in those models.

In addition to the radar signal's phase, the model should also be able to account for the polarimetric coupling between the antenna patterns and the target scattering. Although this aspect is always emphasized in texts related to polarimetric radar,[11] our argument is that the polarization coupling effect is important in single-channel radar systems as well (i.e., systems equipped with only one Tx and one Rx antenna) and must always be taken into account in modeling strip-map SAR systems operating with wide-beam antennas, both in near- and far-field configurations. These issues have been discussed in some of our previous work. Thus, Dogaru[12] made the analysis of a near-field wide-beam GPR UWB SAR system in the presence of a point target, whereas Dogaru and Le[13] dealt with a more complex STTW radar-scattering scene placed in the far field. In the current report, we generalize this analysis to near-field scenarios in the presence of arbitrary targets.

To formulate a general model of the radar signal, we start by introducing the main concepts and equations involved in this analysis. One of these concepts is the effective length of the antenna $\mathbf{h}$,[11,14] which is a vector quantity that characterizes the polarimetric antenna patterns. This vector has two components: h_θ and h_ϕ. (Throughout this report, we use the θ and ϕ subscripts for the vertical and horizontal polarization, respectively.) The electric field incident on the target $\mathbf{E}_i$ is related to the effective length of the Tx antenna by[11]

$$\mathbf{E}_i = \frac{jZ_0 I_T}{2\lambda R_T} e^{-jkR_T} \mathbf{h}_T , \tag{7}$$

while the open-circuit voltage at the Rx antenna V_R is related to its effective length by[11]

$$V_R = \mathbf{h}_R^T \mathbf{E}_s . \tag{8}$$

In these equations, I_T is the current at Tx antenna terminals, $\mathbf{E}_s$ is the scattered electric field at the Rx antenna, and Z_0 is the free-space impedance. Throughout the rest of this report, we use the subscripts T for "transmitter" and R for "receiver". However, in situations where the symbols involve too many subscripts, we use T and R as superscripts; the difference between the two cases should be clear from the context. In Eq. 8, the superscript T stands for matrix transpose. On a different note, the derivations in this report use the definition of $\mathbf{h}$ for the Tx found in Mott,[11]

which differs from the one in Balanis,[14] who takes a minus sign in Eq. 7. One important feature of typical antenna patterns is that in directions away from the principal planes (also known as the E- and H-planes[14]), any antenna generates a cross-polarized field, meaning that both elements of **h** are nonzero. This observation is especially relevant to radar applications that use wide-beam antennas, such as strip-map SAR imaging at low frequencies.

Another crucial concept that accounts for the polarimetric coupling is the scattering matrix of the target.[7] This is defined as

$$\mathbf{S} = \begin{bmatrix} S_{\theta\theta} & S_{\theta\phi} \\ S_{\phi\theta} & S_{\phi\phi} \end{bmatrix}, \tag{9}$$

where $S_{pq} = R_R e^{jkR_R} \dfrac{E_{s,p}}{E_{i,q}}$ (the indexes p and q stand for either θ or ϕ). While this is the general definition of the scattering matrix elements (for arbitrary range), in the far-field case we take the limit of these expressions as $R_R \to \infty$. Their relation to the polarimetric RCS is $\sigma_{pq} = 4\pi \left| S_{pq} \right|^2$. Note though that the **S** matrix elements offer a more complete characterization of target scattering than the polarimetric RCS, since they include the phases as well as the magnitudes.

Based on the previous equations, we obtain the radar-received signal as

$$V_R = \frac{jZ_0 I_T}{2\lambda R_R R_T} e^{-jk(R_R + R_T)} \mathbf{h}_R^T \mathbf{S} \mathbf{h}_T \,. \tag{10}$$

For generality, in this section we consider the case of bistatic radar, with separate (and possibly different) Tx and Rx antennas. Equation 10 is valid at one frequency (or narrowband radar waveforms). In the case of wideband waveforms, Eq. 10 can be applied frequency-by-frequency, followed by an inverse Fourier transform.

The quantities I_T and V_R are related to the transmitted and received powers by the following equations[14]:

$$P_T = \frac{Z_A^T \left| I_T \right|^2}{2}, \qquad P_R = \frac{\left| V_R \right|^2}{8 Z_A^R}, \tag{11}$$

where Z_A^T and Z_A^R are the input impedances of the Tx and Rx antennas, respectively. More precisely, P_T is the power radiated by the Tx antenna, while P_R is the power delivered to the load by the Rx antenna. In writing Eq. 11, we assumed that both antennas are matched to the generator/load and the feed lines, although

this assumption is not critical (mismatch losses can be separately introduced in the signal equation). Combining Eqs. 10 and 11, we obtain

$$P_R = \frac{P_T}{16\lambda^2 R_R^2 R_T^2} \frac{Z_0^2}{Z_A^R Z_A^T} \left| \mathbf{h}_R^T \mathbf{S} \mathbf{h}_T \right|^2, \tag{12}$$

which starts resembling the classic radar equation. Moreover, the magnitudes of the effective lengths are related to the antenna directivities (D_θ and D_ϕ) by the following equations[14]:

$$\left| h_{\theta,\phi} \right| = \lambda \sqrt{D_{\theta,\phi}} \sqrt{\frac{Z_A}{\pi Z_0}}. \tag{13}$$

Upon inserting Eq. 13 into Eq. 12 and ignoring the polarimetric coupling, we obtain

$$P_R = P_T \frac{D_R D_T \lambda^2 \sigma}{(4\pi)^3 R_R^2 R_T^2}, \tag{14}$$

which is exactly the radar equation for bistatic radar configurations.[7] However, Eq. 12 is a more accurate model of the radar signal power than Eq. 14, because it accounts for the polarimetric coupling between antenna patterns and target scattering.

While Eq. 10 offers a complete characterization of the complex radar signal, typical RF system measurements consist of signal power and phase rather than currents and voltages.[15] Therefore, it is more convenient to obtain equivalent formulas that preserve the phase information, but involve the powers (P_T and P_R) and directivities (D_θ and D_ϕ), rather than I_T, V_R, and $\mathbf{h}$, which are less familiar to the radar engineer. For this purpose, we take the phase of I_T as reference (meaning its phase is zero) and write $I_T = \sqrt{\frac{2P_T}{Z_A^T}}$. Then, we have

$$\mathbf{h} = \begin{bmatrix} h_\theta \\ h_\phi \end{bmatrix} = \lambda \sqrt{\frac{Z_A}{\pi Z_0}} \begin{bmatrix} \sqrt{D_\theta} e^{j\psi_\theta} \\ \sqrt{D_\phi} e^{j\psi_\phi} \end{bmatrix} = \lambda \sqrt{\frac{Z_A}{\pi Z_0}} \mathbf{D}^{SQ}. \tag{15}$$

In this equation, which is valid for both Tx and Rx antennas, we introduced the symbol $\mathbf{D}^{SQ}$ (SQ stands for the "square-root" of the directivities), while ψ_θ and ψ_ϕ represent the phases of h_θ and h_ϕ, respectively. Any complete characterization of the antenna pattern, by either measurements or modeling, should include the quantities D_θ, D_ϕ, ψ_θ, and ψ_ϕ, which are described compactly by $\mathbf{D}^{SQ}$. For example,

when modeling an antenna with the Feko software, these quantities can be readily found in tabulated form in the output files, at the frequencies and angles of interest. We can then rewrite Eq. 10 as

$$V_R = \frac{j\lambda\sqrt{2Z_A^R P_T}}{2\pi R_R R_T} e^{-jk(R_R+R_T)} \left(\mathbf{D}_R^{SQ}\right)^T \mathbf{S}\mathbf{D}_T^{SQ}. \tag{16}$$

At the receiver end, we have $V_R = \sqrt{8P_R Z_A^R} e^{j\psi_R}$, where ψ_R is the phase of the received voltage V_R. If instead of V_R we want to measure or compute the signal $X = \frac{V_R}{\sqrt{8Z_A^R}} = \sqrt{P_R} e^{j\psi_R}$, we obtain

$$X = \frac{j\lambda\sqrt{P_T}}{4\pi R_R R_T} e^{-jk(R_R+R_T)} \left(\mathbf{D}_R^{SQ}\right)^T \mathbf{S}\mathbf{D}_T^{SQ} \ . \tag{17}$$

Another possible quantity of interest is $Y = \frac{X}{\sqrt{P_T}} = \sqrt{\frac{P_R}{P_T}} e^{j\psi_R}$, which is an alternate version of X, normalized to the Tx power. This signal is given by

$$Y = \frac{j\lambda}{4\pi R_R R_T} e^{-jk(R_R+R_T)} \left(\mathbf{D}_R^{SQ}\right)^T \mathbf{S}\mathbf{D}_T^{SQ}. \tag{18}$$

By definition, the signal Y has a magnitude equal to the square root of the Rx-to-Tx-power ratio, and a phase equal to the difference between the Rx and Tx signal phases. As such, it provides all the relevant information related to the radar-sensing scenario and can be used in subsequent coherent processing schemes. In addition, the signal X, which is scaled up by the Tx power, provides an absolute measure of the radar signal's magnitude and phase.

The received power can be computed as

$$P_R = \frac{|V_R|^2}{8Z_A^R} = P_T \frac{\lambda^2}{16\pi^2 R_R^2 R_T^2} \left| \left(\mathbf{D}_R^{SQ}\right)^T \mathbf{S}\mathbf{D}_T^{SQ} \right|^2. \tag{19}$$

The equations modeling the radar signal developed in this section are generally valid for both near- and far-field configurations. The main difference between the two consists of the scattering matrix and polarimetric RCS definitions: the far-field version considers these quantities in the limit $R \to \infty$. The antenna effective lengths and directivities are quantities characterizing the antenna patterns in the far-field region. However, their formulations in Eqs. 7 and 8 are also valid for most of

the near-field scenarios of interest, as long as the antennas have relatively small sizes and the target is placed at least several wavelengths away, outside their reactive field region.[14]

4. Near-Field Target Scattering Characterization Using the AFDTD Modeling Software

In this section, we examine ways to exploit data provided by EM modeling software for the calculations involved in Eqs. 17 and 18, for near-field radar-sensing configurations. The key quantities required by these equations are $\mathbf{D}_T^{SQ}$ and $\mathbf{D}_R^{SQ}$, which characterize the Tx and Rx antennas, respectively, and $\mathbf{S}$, which characterizes the target scattering. The procedure presented here assumes that the antenna patterns and target scattering are modeled separately (alternatively, one can mix simulated and measured data for either of these stages). As already discussed, antenna modeling software typically provides all the ingredients necessary for the computation of $\mathbf{D}^{SQ}$. In this section, we focus on the derivation of $\mathbf{S}$ based on EM modeling data. More specifically, we develop a procedure of extracting $\mathbf{S}$ from AFDTD near-field simulations involving infinitesimal (or Hertzian) dipoles,[14] which are the most common type of antennas used by this software package.

In far-field configurations, finding $\mathbf{S}$ via EM models is a straightforward task—one can use plane-wave incident fields with each polarization (θ and ϕ) separately and evaluate the plane-wave scattered field in both polarizations for each incident polarization, respectively. In fact, AFDTD (as well as other EM modeling software packages) outputs the $\mathbf{S}$ matrix elements directly for far-field configurations, with the proper phases and power normalizations.[1]

The procedure is more complicated for near-field configurations, where it is rather difficult to find antennas that transmit purely polarized fields (with either θ or ϕ polarization), so the $\mathbf{S}$ elements cannot be evaluated by the same direct method as in the far field. To solve this problem, let us assume we make two separate radar measurements involving the same sensing geometry, with Tx antennas that have linearly independent polarizations (for now, the Rx antenna stays unchanged). These measurements are characterized by currents I_{T1} and I_{T2} and non-collinear effective length vectors $\mathbf{h}_{T1} = \begin{bmatrix} h_{\theta 1}^T \\ h_{\phi 1}^T \end{bmatrix}$ and $\mathbf{h}_{T2} = \begin{bmatrix} h_{\theta 2}^T \\ h_{\phi 2}^T \end{bmatrix}$, respectively. The voltages obtained at the receiver in the two measurements are

$$V_{R1,2} = \frac{jZ_0}{2\lambda R_R R_T} e^{-jk(R_R+R_T)} \mathbf{h}_R^T \mathbf{S} \mathbf{h}_{T1,2} I_{T1,2} \,. \tag{20}$$

The primary quantity evaluated at the receiver by the AFDTD software is the electric field vector $\mathbf{e}_R = \begin{bmatrix} E_\theta^R \\ E_\phi^R \end{bmatrix}$ rather than the voltage, so a more natural way of describing the results of the two radar simulations is

$$\mathbf{e}_{R1,2} = \frac{jZ_0}{2\lambda R_R R_T} e^{-jk(R_R+R_T)} \mathbf{S}\mathbf{h}_{T1,2} I_{T1,2} . \tag{21}$$

In matrix format, this equation can be written as

$$\mathbf{E}_R = \frac{jZ_0}{2\lambda R_R R_T} e^{-jk(R_R+R_T)} \mathbf{S}\mathbf{H}_T \mathbf{I}_T , \tag{22}$$

where $\mathbf{E}_R = \begin{bmatrix} E_{\theta 1}^R & E_{\theta 2}^R \\ E_{\phi 1}^R & E_{\phi 2}^R \end{bmatrix}$, $\mathbf{H}_T = \begin{bmatrix} h_{\theta 1}^T & h_{\theta 2}^T \\ h_{\phi 1}^T & h_{\phi 2}^T \end{bmatrix}$, and $\mathbf{I}_T = \begin{bmatrix} I_{T1} & 0 \\ 0 & I_{T2} \end{bmatrix}$. The matrix **S** can then be extracted from Eq. 22 as

$$\mathbf{S} = \frac{2\lambda R_R R_T}{jZ_0} e^{jk(R_R+R_T)} \mathbf{E}_R \mathbf{I}_T^{-1} \mathbf{H}_T^{-1} . \tag{23}$$

The requirement to have non-collinear vectors $\mathbf{h}_{T1}$ and $\mathbf{h}_{T2}$ simply ensures that the inverse of the matrix $\mathbf{H}_T$ exists.

A practical procedure of evaluating **S** from AFDTD near-field models involves using two infinitesimal dipoles with unit dipole moment $I_T l$ oriented in the θ and ϕ directions (θ now stands for "1" and ϕ stands for "2") in separate simulations, and measuring the θ and ϕ components of the electric field at the Rx location for each Tx polarization. The results of these simulations are combined in the matrix $\mathbf{E}_D^{SS} = \begin{bmatrix} E_{\theta\theta}^R & E_{\theta\phi}^R \\ E_{\phi\theta}^R & E_{\phi\phi}^R \end{bmatrix}$, where we used the subscript *D* for "dipoles" and the *SS* superscript for "spherical-spherical" to indicate that the quantities characterizing both the Tx and the Rx are expressed in spherical coordinates. For an infinitesimal dipole antenna, the effective length polarimetric matrix **H** expressed in spherical coordinates (θ and ϕ) is[14]

$$\mathbf{H} = \begin{bmatrix} -l & 0 \\ 0 & -l \end{bmatrix}, \tag{24}$$

where l is the dipole length (note that if we followed the effective length vector definition used by Balanis,[14] l would appear with positive signs in Eq. 24). Then

$$\mathbf{I}_T^{-1}\mathbf{H}_T^{-1} = \begin{bmatrix} -(I_{T1}l)^{-1} & 0 \\ 0 & -(I_{T2}l)^{-1} \end{bmatrix} = -\begin{bmatrix} 1 & 0 \\ 0 & 1 \end{bmatrix}, \tag{25}$$

and Eq. 23 becomes

$$\mathbf{S} = \frac{j2\lambda R_R R_T}{Z_0} e^{jk(R_R+R_T)} \mathbf{E}_D^{SS} . \tag{26}$$

The last equation shows a one-to-one correspondence between the elements of the $\mathbf{E}_D^{SS}$ matrix (which is evaluated with the AFDTD software) and the elements of the scattering matrix **S**. The latter can then be computed simply as

$$S_{pq} = \frac{j2\lambda R_R R_T}{Z_0} e^{jk(R_R+R_T)} E_{pq}^R , \tag{27}$$

with p and q standing for θ or ϕ.

Although AFDTD allows the direct implementation of dipoles with arbitrary orientations, it is more convenient to run simulations with the dipoles oriented along the Cartesian directions, x, y, and z. Similarly, at the receiver, we measure directly the components x, y, and z of the electric field, so we would like to re-derive Eq. 26 using these components rather than the spherical components. For this purpose, we use the transformation matrices from spherical to Cartesian coordinates (notation $\mathbf{Q}^{S\to C}$) and from Cartesian to spherical coordinates (notation $\mathbf{Q}^{C\to S}$). We have[14]

$$\mathbf{Q}^{C\to S} = \begin{bmatrix} \cos\theta\cos\phi & \cos\theta\sin\phi & -\sin\theta \\ -\sin\phi & \cos\phi & 0 \end{bmatrix}, \tag{28}$$

and $\mathbf{Q}^{S\to C} = \left(\mathbf{Q}^{C\to S}\right)^T$. Additionally, $\mathbf{Q}^{C\to S}\mathbf{Q}^{S\to C} = \begin{bmatrix} 1 & 0 \\ 0 & 1 \end{bmatrix}$. We can then write

$$\mathbf{E}_D^{SS} = \mathbf{Q}_R^{C\to S}\mathbf{E}_D^{CC}\mathbf{Q}_T^{S\to C} , \tag{29}$$

where $\mathbf{E}_D^{CC} = \begin{bmatrix} E_{xx}^R & E_{xy}^R & E_{xz}^R \\ E_{yx}^R & E_{yy}^R & E_{yz}^R \\ E_{zx}^R & E_{zy}^R & E_{zz}^R \end{bmatrix}$ (superscript *CC* stands for "Cartesian-Cartesian"). Here, the notation E_{pq}^R means the p-component of the electric field measured at the Rx when we use a q-oriented dipole as Tx, where p and q can be either of x, y, or z. The angles involved in the coordinate transformation matrices **Q** are evaluated at the Tx or Rx locations, according to the subscript denoting those matrices.

Based on $\mathbf{E}_D^{CC}$, the scattering matrix is computed by the following formula

$$\mathbf{S} = \frac{j2\lambda R_R R_T}{Z_0} e^{jk(R_R+R_T)} \mathbf{Q}_R^{C\to S} \mathbf{E}_D^{CC} \mathbf{Q}_T^{S\to C}, \tag{30}$$

This completes the characterization of the scattering matrix of a target in the near field. To implement the procedure with the AFDTD software, we need to run three separate simulations using Tx dipoles in the *x*, *y*, and *z* orientations, respectively, and record the electric field components at the Rx location for each case. Once we build the $\mathbf{E}_D^{CC}$ matrix, we use Eq. 30 to find **S**. The other quantities in Eq. 30 (including the angles required by the coordinate transformation matrices) can be readily derived from the sensing geometry. The dipole simulations used in the calculation of **S** must use exactly the same geometry as the one involving the actual antennas. If we change the antenna positions relative to the target, **S** changes and we need to repeat the dipole-based evaluation procedure for the new set of coordinates.

After finding **S**, we can compute the complex signal or power received from the same target with arbitrary Tx and Rx antennas by using one of the Eqs. 16–19, as long as we know the $\mathbf{D}^{SQ}$ vectors characterizing those antennas. If we do not require the explicit evaluation of the scattering matrix, the voltage V_R, the signal Y, and the received power P_R can be computed directly by the following formulas, respectively:

$$V_R = -\frac{\lambda^2 \sqrt{2Z_A^R P_T}}{\pi Z_0} \left(\mathbf{D}_R^{SQ}\right)^T \mathbf{Q}_R^{C\to S} \mathbf{E}_D^{CC} \mathbf{Q}_T^{S\to C} \mathbf{D}_T^{SQ}, \tag{31}$$

$$Y = -\frac{\lambda^2}{2\pi Z_0} \left(\mathbf{D}_R^{SQ}\right)^T \mathbf{Q}_R^{C\to S} \mathbf{E}_D^{CC} \mathbf{Q}_T^{S\to C} \mathbf{D}_T^{SQ}, \tag{32}$$

$$P_R = P_T \frac{\lambda^4}{4\pi^2 Z_0^2} \left| \left(\mathbf{D}_R^{SQ}\right)^T \mathbf{Q}_R^{C\to S} \mathbf{E}_D^{CC} \mathbf{Q}_T^{S\to C} \mathbf{D}_T^{SQ} \right|^2. \tag{33}$$

5. Numerical Examples

The theory developed so far in this study would be incomplete without a numerical example to validate the procedure. For this purpose, besides the Tx infinitesimal dipoles, we consider another type of antenna that can be implemented directly in the AFDTD software—namely, a rectangular aperture (RA) with uniform surface current density.[14] The validation consists of computing the scattering by a target with the RA antenna as Tx by (1) directly modeling the entire problem with the RA

antenna and (2) obtaining the matrix **S** from dipole-based simulations, then using Eq. 16 to compute the received signal with the RA antenna. In the process, we also evaluate the target's near-field RCS for all polarization combinations.

The sensing geometry is described in Fig. 2. The target is a PEC plate with dimensions 1 m × 0.6 m, in vertical orientation (*y*-*z* plane). The radar is placed at a distance 5 m × 2.8 m × 2 m with respect to the center of the plate, in the *x*, *y*, and *z* directions, respectively. The antenna is a rectangular aperture in the *y*-*z* plane (dimensions 0.15 m × 0.3 m), with uniform-density magnetic surface currents oriented in the *z* direction, producing horizontal polarization. For this monostatic geometry, we have $R_T = R_R = R \cong 6$ m.

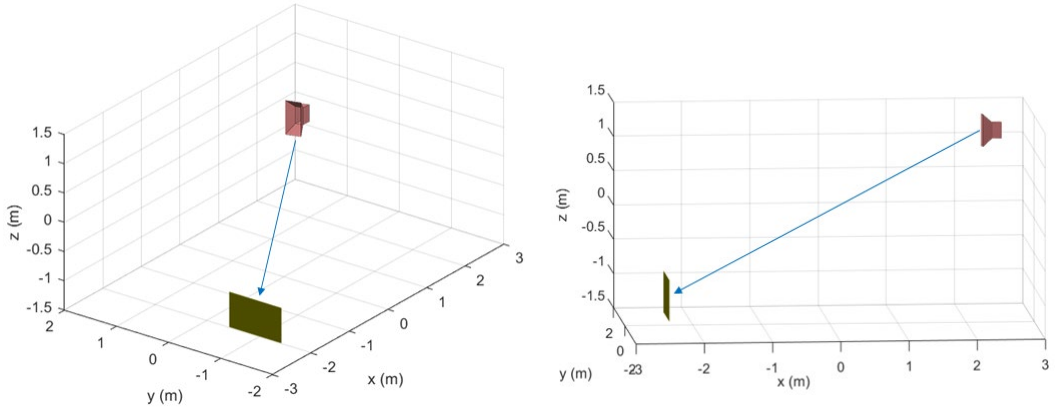

Fig. 2 Geometry of the near-field radar-sensing configuration used for validating the indirect near-field RCS calculation via the dipole method described in Section 4

As previously described, we first run the simulations with dipoles oriented in the three Cartesian directions, and placed at the real antenna's phase center, and record the electric field Cartesian components at the Rx location. The result of these three simulations is the $\mathbf{E}_D^{CC}$ matrix. Next, we run the simulation with the RA antenna as Tx and measure the Cartesian components of the electric field vector at two locations: in the center of the target ($\mathbf{E}_{iA}^{C}$) and back at the Rx ($\mathbf{E}_{RA}^{C}$). Let $\mathbf{E}_{iA}^{S}$ and $\mathbf{E}_{RA}^{S}$ be the spherical coordinate counterparts of these two vectors. (The notations in this section allow us to differentiate an electric field vector from a matrix made of multiple electric field vectors by using a single superscript in the former case, e.g., $\mathbf{E}_{RA}^{C}$, vs. a double superscript in the latter case, e.g., $\mathbf{E}_D^{CC}$.)

Knowing the values of the electric field vectors in the center of the target and at the Rx enables a streamlining of the procedure described in Section 4. Thus, according to the scattering matrix definition, we have

$$\mathbf{E}_{RA}^{S} = \frac{e^{-jkR}}{R}\mathbf{S}\mathbf{E}_{iA}^{S} = \frac{e^{-jkR}}{R}\mathbf{S}\mathbf{Q}_{T}^{C\to S}\mathbf{E}_{iA}^{C}. \tag{34}$$

$$\mathbf{E}_{RA}^{C} = \mathbf{Q}_{R}^{S\to C}\mathbf{E}_{RA}^{S} = \frac{e^{-jkR}}{R}\mathbf{Q}_{R}^{S\to C}\mathbf{S}\mathbf{Q}_{T}^{C\to S}\mathbf{E}_{iA}^{C}. \tag{35}$$

One possible way to perform the validation is to compute the **S** matrix by the dipole method, plug its elements into Eq. 35, and compare the results of this formula (the components of $\mathbf{E}_{RA}^{C}$) with the direct RA antenna simulation results. However, a more direct way to compute $\mathbf{E}_{RA}^{C}$ is to replace the expression of **S** from Eq. 30 into Eq. 35, and obtain

$$\mathbf{E}_{RA}^{C} = \frac{j2\lambda R}{Z_0}e^{jkR}\mathbf{E}_{D}^{CC}\mathbf{E}_{iA}^{C}. \tag{36}$$

Consequently, this validation method does not require the explicit evaluation of the scattering matrix elements. The results of the comparison between the two methods for the three Cartesian components of the electric field as a function of frequency are shown in Fig. 3. The match is reasonably good, with the more significant differences occurring in regions of low field intensity. Possible sources of errors are numerical dispersion in the finite-difference time-domain EM solver[16] (which is completely unrelated to the method outlined in this report); and for targets of large extent, the fields generated by dipoles do not display pure polarization (either $\theta-$ or $\phi-$ oriented) properties across the entire target surface (in other words, the matrix **H** in Eq. 24 is no longer diagonal).

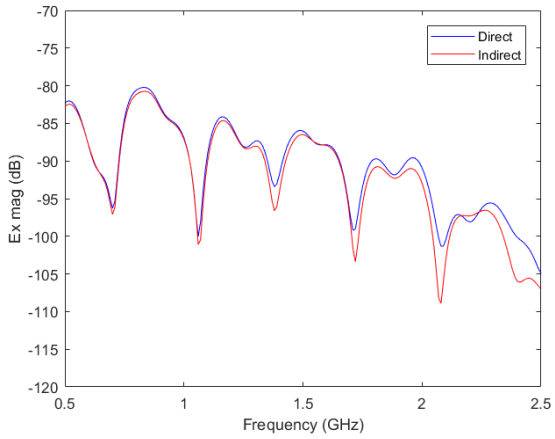

(a)

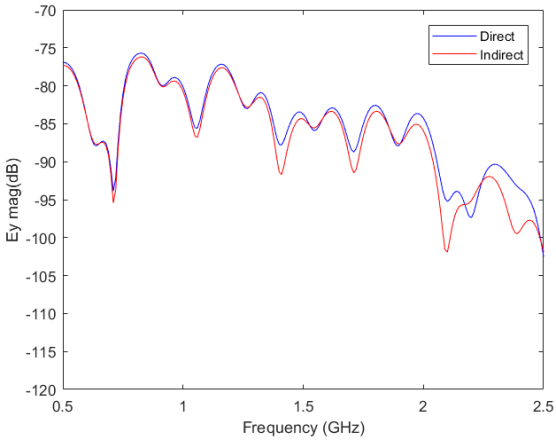

(b)

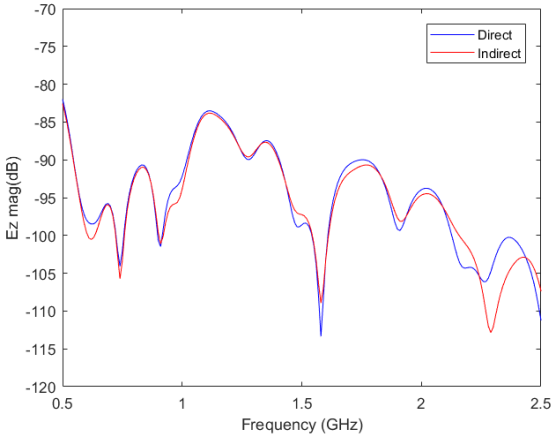

(c)

Fig. 3 Comparison of electric field magnitudes at the receiver obtained by the direct and indirect methods: (a) E_x component; (b) E_y component; and (c) E_z component

Equation 30 allows the calculation of the scattering matrix elements and the RCS for all polarization combinations. The results of the near-field calculations are shown in Fig. 4, together with their far-field counterparts obtained directly by AFDTD simulations of the same target, with Tx and Rx placed at the same angles as in the near-field case.

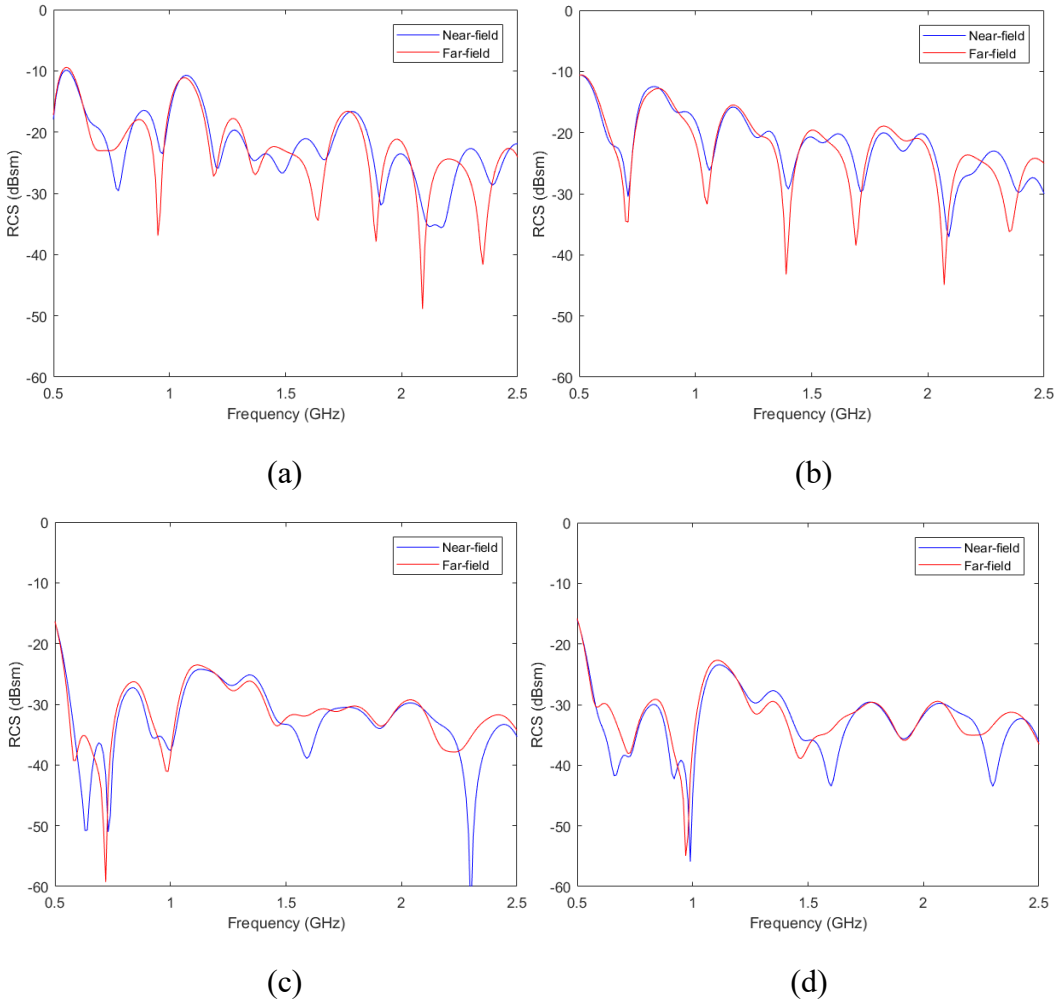

Fig. 4 Comparison between the near-field and far-field RCS of a rectangular plate of dimensions 1 m × 0.6 m, computed by AFDTD simulations for (a) V-V (θ–θ) polarization; (b) H-H (ϕ–ϕ) polarization; (c) V-H (θ–ϕ) polarization; and (d) H-V (ϕ–θ) polarization

We can clearly see differences between the near- and far-field RCS in Fig. 4; these differences typically become larger as the frequency is increased. However, for this oblique incidence angle, the far-field RCS is not consistently larger than the near-field RCS (in fact, they both follow similar trends on the average), unlike in the normal incidence case examined in Section 2. One can also notice some differences between the vertical-horizontal (V-H) and horizontal-vertical (H-V) polarization RCS, due to the slightly bistatic sensing geometry (note that the Tx and Rx are not

exactly collocated, but shifted by 0.3 m in the x direction with respect to one another).

Finally, we verify the analytic formula for near-field RCS of a circular PEC plate (Eq. 3) vs. near-field AFDTD simulations. In the case of normal incidence to a vertical plate, only the vertical-vertical (V-V) RCS is relevant (since the horizontal-horizontal [H-H] RCS is identical), so we only need to run the AFDTD model with a z-oriented dipole. Figure 5 shows the results of this comparison for a plate with radius a = 0.5 m, placed at a 5-m range. In the same graph, we included the far-field RCS of the same plate at normal incidence, obtained by both far-field AFDTD simulation and analytic formula (Eq. 4). As before, the main point of this comparison is to illustrate the divergence between the near- and far-field RCS as the frequency increases.

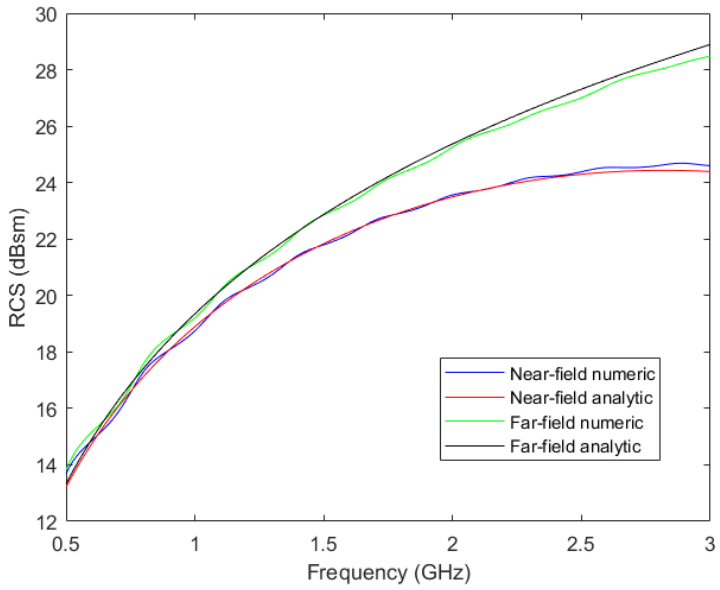

Fig. 5 Comparison between the near- and far-field RCS of a circular plate of radius 0.5 m at 5-m range, computed analytically and by AFDTD simulations

6. Conclusions

The purpose of this report is to illustrate the development of near-field radar modeling techniques able to produce the power-calibrated radar-received signal for arbitrary antennas and target configurations. To ensure the model's accuracy and fidelity, the final results must preserve the signal's phase, the near-field effects (due primarily to the spherical wavefront curvature), and the polarimetric coupling effects between the antenna patterns and target scattering. As such, the radar-sensing scenario simulations can provide essential information to the radar designer in terms of performance prediction and system parameter trade space.

Throughout this study, we emphasized the differences between the near- and far-field models, showing that the former requires a more careful description of the sensing scenario, which must specifically include the radar antennas and their polarimetric patterns. After introducing the concept of near-field RCS in Section 2, we developed a general version of the radar equation in Section 3. This version, which preserves the phase and the polarimetric coupling effects, offers a complete description of the radar-received signal that can be used in complex processing algorithms such as SAR image formation.

After acknowledging that currently available EM modeling software is not capable of directly simulating the full near-field radar-sensing scenario, in Section 4 we developed an indirect procedure to accomplish this goal based primarily on the AFDTD solver. In this procedure, we perform target-scattering simulations using infinitesimal dipoles with unit dipole moments, which are readily implemented as the simplest form of Tx antennas by AFDTD, and evaluate the target's scattering matrix. This is used in conjunction with the antenna models or measurements (which must be performed separately outside the AFDTD software) to produce the radar-received signals in the presence of those antennas.

A simple numerical example in Section 5 demonstrates the validity of this simulation method. Although this work is primarily theoretical, it hopefully lays the foundations for future advanced models of complex radar-sensing scenarios that prove useful in system analysis and design.

7. References

1. Dogaru T. AFDTD user's manual. Army Research Laboratory (US); 2010 Mar. Report No.: ARL-TR-5145.
2. Dogaru T. NAFDTD – a near-field finite difference time domain solver. Army Research Laboratory (US); 2012 Sep. Report No.: ARL-TR-6110.
3. Leidos Products Web Page [accessed 2021 April]. https://www.leidos.com/products.
4. Altair Feko Software Web page [accessed 2021 April]. https://www.altair.com/feko/.
5. Soumekh M. Synthetic aperture radar signal processing. Wiley; 1999.
6. Dogaru T. Synthetic aperture radar for helicopter landing in degraded visual environments. Army Research Laboratory (US); 2018 Dec. Report No.: ARL-TR-8595.
7. Richards M, Scheer J, Holm W. Principles of modern radar – basic principles. SciTech Publishing; 2010.
8. Pouliguen P, Hemon R, Bourlier C, Damiens JF, Saillard J. Analytical formulae for radar cross section of flat plates in near field and normal incidence. Prog Electromag Res B. 2008;9:263–279.
9. Knott E, Shaeffer J, Tuley M. Radar cross section. Artech; 1993.
10. Melvin W, Scheer J. Principles of modern radar–advanced techniques. SciTech Publishing; 2013.
11. Mott H. Remote sensing with polarimetric radar. Wiley; 2007.
12. Dogaru T. Imaging study for small-UAV-mounted ground penetrating radar: part III – a multi-static approach. CCDC Army Research Laboratory (US); 2019 Mar. Report No.: ARL-TR-8654.
13. Dogaru T, Le C. Through the wall radar simulations using polarimetric antenna patterns. Army Research Laboratory (US); 2012 Mar. Report No.: ARL-TR-5951.
14. Balanis C. Antenna theory–analysis and design. Wiley; 1997.
15. Collin R. Foundations for microwave engineering. IEEE Press; 2001.
16. Taflove A, Hagness S. Computational electrodynamics: the finite-difference time-domain method. Artech; 2000.

List of Symbols, Abbreviations, and Acronyms

ARL	Army Research Laboratory
DEVCOM	US Army Combat Capabilities Development Command
EM	electromagnetic
GPR	ground-penetrating radar
H-H	horizontal-horizontal
H-V	horizontal-vertical
PEC	perfect electric conductor
PO	physical optics
RA	rectangular aperture
RCS	radar cross section
RF	radio frequency
Rx	receiver
SAR	synthetic aperture radar
STTW	sensing through the wall
Tx	transmitter
UWB	ultra-wideband
V-H	vertical-horizontal
V-V	vertical-vertical

1 (PDF)	DEFENSE TECHNICAL INFORMATION CTR DTIC OCA
1 (PDF)	DEVCOM ARL FCDD RLD DCI TECH LIB
5 (PDF)	DEVCOM ARL FCDD RLS RU A SULLIVAN T DOGARU C LE B PHELAN C KENYON